

LRP 506/94

September 1994

**SPATIO-TEMPORAL POWDER
FORMATION AND TRAPPING IN RF
SILANE PLASMAS USING 2-D
POLARIZATION-SENSITIVE LASER
SCATTERING**

J.-L. Dorier, Ch. Hollenstein, A.A. Howling

Contributed paper to the 41st
National Symposium of the
American Vacuum Society in
Denver 24-28 October 1994

SPATIO-TEMPORAL POWDER FORMATION AND TRAPPING IN RF SILANE
PLASMAS USING 2-D POLARIZATION-SENSITIVE LASER SCATTERING

J.-L. Dorier, Ch. Hollenstein, and A. A. Howling
Centre de Recherches en Physique des Plasmas
Ecole Polytechnique Fédérale Lausanne
21 Av. des Bains, CH-1007 Lausanne, Switzerland.

ABSTRACT

Powder formation studies in deposition plasmas are motivated by the need to reduce contamination in the plasma and films. Models for the forces acting upon particles in rf discharges suffer from a lack of quantitative experimental data for comparison in the case of silane-containing plasmas. In this work, a cross-section of the parallel-plate capacitor discharge is illuminated with a polarized beam-expanded laser and global spatio-temporal scattered light and extinction are recorded by CCD cameras. Spatially-regular periodic bright/dark zones due to constructive/destructive Mie interference are visible over large regions of the powder layers, which shows the uniform nature of particle growth in silane plasmas. For particles trapped in an argon plasma, as for steady-state conditions in silane, spatial size segregation is demonstrated by fringes which reverse according to the polarisation of scattered light. The method allows a self-consistent estimation of particle size and number density throughout the discharge volume from which strong particle Coulomb coupling ($\Gamma > 40$) is suggested to influence powder dynamics. Correction must be made to the plasma emission profile for the extinction by powder. In conclusion, this global diagnostic improves understanding of particle growth and dynamics in silane rf discharges and provides experimental input for testing the validity of models.

1) INTRODUCTION

Contamination by particles in plasma reactors used for deposition, etching or sputtering [1, 2] has motivated extensive theoretical and experimental studies of powder formation and trapping in low pressure glow discharges. From another point of view, the plasma synthesis of nanosized particles is interesting for materials applications [3]. Powder formation can be commensurate with good quality film at high deposition rate in terms of better rf power coupling with lower sheath potential [4] provided that direct contamination of the deposited films by particles is avoided.

Many theoretical studies have addressed various questions such as particle formation [5, 6], charging [6-10], transport [6, 11-14], and the consequences of particles in plasmas [6, 15, 16]. Particle coupling [6, 17] and reactor geometry [6, 18] also influence particle trapping. Some experimental comparisons exist but there is often a lack of quantitative data, particularly in the case of silane-containing plasmas. Advanced in-situ diagnostic tools are therefore required for a better understanding of the particle formation and dynamics, as well as for process control [1, 19].

In most experiments, the particles are detected in-situ by laser scattering, where spatial resolution is obtained by moving the reactor or by displacing [20-22] or rastering [1] the laser beam, and time evolution monitoring is constrained to a limited powder volume [23, 24]. Only a few studies attempt to determine the particle size and number density by either angular dissymetry [25], dynamic [26] or polarisation-sensitive light scattering techniques [27, 28], sometimes in correlation with ex-situ TEM measurements [24, 29, 30].

The scattered intensity is a complex convolution of particle size, refractive index and number density [31], and so many studies only use qualitative global 2-D visualization to localise the powder clouds [19, 20, 28, 32, 33] or structures [1].

In this work, we use a polarized expanded laser beam and monitor the global spatio-temporal powder dynamics with scattered and transmitted intensities by CCD cameras. Well-defined periodic and spatial intensity variations due to Mie interference enable the visualization of particle size gradients in the plasma. An iterative procedure is applied to self-consistently estimate the particle size and number density throughout the discharge volume during particle growth. It is also possible to follow the particles during their growth, which is necessary because of the displacement of particle clouds observed for long time developments [23, 32]. The observed powder structures are speculatively interpreted in terms of double layers [34, 35] and particle Coulomb coupling [17, 29, 35, 36, 37].

2) EXPERIMENTAL DESCRIPTION

2.1) Experimental arrangement

Figure 1 shows top and side views of the plasma reactor with the 2-D laser scattering set-up. The reactor consists of two, symmetric stainless steel cylindrical electrodes of diameter 130 mm positioned 27 mm apart in a cubic, grounded vacuum vessel of 400 mm side. The lower, rf electrode has a concentric grounded guard screen of 138 mm diameter and is capacitively coupled through a π -matching circuit to a rf amplifier and generator (30MHz). The input powers used were 3 to 6 W for the experiments described here. The reactor is at ambient temperature to minimise thermal gradients which would perturb the powder dynamics because of thermophoretic forces [20]. It also favors the formation of a large amount of powder at relatively low power.

The gas influx is in the side wall of the chamber and a fine mesh disk in front of the inlet minimises gas drag forces on the powder. The gases used for the present work were pure silane, silane diluted with argon, or pure argon, at a total gas pressure of 0.1 mbar. The reactor windows are positioned at the end of 250 mm long radial ports to avoid any deposition of amorphous silicon film.

An argon ion laser beam at 488 nm wavelength passes through a 4-prism beam expander and a polariser before entering the reactor. The expanded beam is collimated by a rectangular aperture to illuminate a central cross-section of the electrode gap (27 mm height, 1 mm thickness). The polarizer axis is set either in the z (vertical polarization) or y direction (horizontal polarization).

After crossing the reactor the expanded beam is split by a partially reflecting plate and is focused onto a silicon photo-diode for adjusting equal incident intensities in both polarisations. The reflected part is imaged on a screen for the measurement of the vertical extinction profile with a CCD camera. A second CCD camera is positioned in the inter-electrode midplane at 90° with respect to the laser. During successive experiments, this camera records either the two-dimensional scattering profile from the powder suspended in the plasma via an interference filter at 488nm, or the plasma optical emission profile with a 414 nm filter for the SiH* band (which dominates the emission of pure silane plasmas). In the case of scattering measurements a polarizer is also placed in front of the camera. Both CCD cameras outputs are synchronized and connected to a two-channel 8 bit 488 x 384 pixel frame grabber computer board.

2.2) Theory

Elastic light scattering by a spherical, homogeneous particle is described by the Lorentz-Mie theory [31]. For a randomly-distributed ensemble the total scattered intensity is the sum of the individual particle intensities provided that no multiple scattering occurs. For identical particles, the time dependent 2-D scattered power profile measured by camera CCD2 (Fig. 1) is:

$$W_h(x,z,t) \propto N_p \Delta V \Delta \Omega |S_h|^2 I_h \quad (1)$$

and equivalently for W_v , where the indices h and v refer to horizontal and vertical polarisations. All variables depend on x, z and time except ΔV and $\Delta\Omega$ which are fixed by the optical system. The terms S_h , S_v are complex elements of the amplitude scattering matrix [31] and are a function of the complex refractive index \underline{n} , the size parameter ($= 2\pi r(x,z,t) / \lambda$; r is the particle radius and λ the source wavelength) and the scattering angle (90° in our case). N_p is the number density of particles present in the observation volume ΔV , defined by the spatial resolution of the 2-D scattering profile (0.5×0.5 mm) and the thickness of the laser illumination (1 mm). Note that ΔV and the solid angle $\Delta\Omega$ must be sufficiently small for the scattering angle to be close to 90° and for the polarisation purity to be conserved. The incident intensities at the observation volume (I_h , I_v in Eq. (1)) are corrected for any absorption and scattering losses from powder between the source and this volume, according to the transmitted power measurement described below.

The measured transmitted power fraction $T(z,t) / T_0(z)$ is independent of polarisation and, for simple scattering, the extinction is given by :

$$1 - T(z,t) / T_0(z) = 1 - \exp [-C_{\text{ext}} N_p d] \quad (2)$$

where the variables depend on z and t; d is the laser path length at height z and C_{ext} the line-averaged extinction cross-section (sum of scattering and absorption) which depends on the size parameter and \underline{n} .

2.3 Experimental procedure

2-D scattering intensity profiles are measured in consecutive experiments with both source and detector polarizers in the vertical and horizontal direction respectively, along with the transmitted intensity vertical profiles. Apart from their physical content the latter measurements also serve to check reproducibility. The signal evolution is highly reproducible even down to the smallest features. Background intensity frames are subtracted and the transmitted profiles $T(z,t)$ normalised to their values with no powder. The intensity profiles are corrected for the dynamic response of the digitization system.

Since we arrange for $I_h = I_v$ we can define :

$$P(x,z,t) = \frac{W_v - W_h}{W_v + W_h} = \frac{|S_v|^2 - |S_h|^2}{|S_v|^2 + |S_h|^2} \quad (3)$$

which would be equivalent to the degree of linear polarisation for the case of unpolarised incident light. Note that P is a function of the size parameter and \underline{n} only, and S_v and S_h , which also determine C_{ext} , are calculated using the BHMIE algorithms [31]. A realistic estimation of particle size requires that the particle development be followed from the beginning because P is a multi-valued function of the size parameter (see figure 2 (a) below). Quantitative, instantaneous measurements of particle size with this technique on an already-formed plasma/particle system are therefore not uniquely determinable without additional information.

However, spatial variations of P can certainly be attributed to spatial changes of the dominant particle size.

Assuming that the particle size never decreases, it is found [27] that there is no unique refractive index which can describe the time variation of P . Therefore we must allow for a changing refractive index $\underline{n}(r)$ with particle growth. The iterative procedure described in ref. [27] (summarized on figure 2 (b)) is followed to self-consistently determine the parameters $\{N_p, r, \underline{n}\}$ as a function of time in elementary volumes corresponding to different points on the digitized frames. This procedure is iterated until a reasonably-accurate self-consistent agreement is found for the measured values of $\{W_v, W_h, T / T_0\}$ in terms of the particle parameters $\{\underline{n}, r, N_p\}$ over the whole time period investigated. Figure 2 (a) shows the simulated P and the relative scattering intensities $|S_h|^2$ and $|S_v|^2$ as a function of particulate radius, with the concomitant size-dependent refractive index. These data are assumed to describe the size dependence of the scattering at any position and time, within the limitations described below, and are used as a database for the measurements presented below.

2.4) Advantages and limitations of the technique

The method described is non-perturbative and gives in-situ, self-consistent spatially-resolved results without requiring any ex-situ measurements. Boufendi *et al* [24] have demonstrated that particles are mono-sized during the early stage of development. Moreover, since the Rayleigh scattering cross-section varies as r^6 for the smallest particles and at least as r^2 for larger particles [31], our assumption of identical particles is justifiable by considering that light scattering from the initial class of particles will dominate the detected signal during the particle development investigated here. There is also a limitation intrinsic to the method: N_p is calculated from extinction profiles in which we assume the same particle size along the laser path at a given height.

3) RESULTS AND DISCUSSION

3.1) Time development of powder in pure silane cw plasma

Figure 3 shows the time evolution of the light scattering frames for both vertical and horizontal laser polarisation with the corresponding vertical extinction profiles. These data are samples from two runs of 69 images taken at 1.5 s intervals covering a time range of 102 s from the plasma ignition. In the right column we represent a pseudo-color image construction of the corresponding degree of polarisation P , calculated using equation Eq. (3). P is represented at each point where both scattered intensities were larger than 4 % of the maximum value, to exclude background noise. On the same frames are also represented contours of zones where W_v is larger, and W_h smaller, than 4 % of the maximum value, which correspond to Rayleigh scattering [31]. In these regions the particle radius is estimated to be less than 15-20 nm. This

figure will be used as a guide-line for the interpretation and presentation of the following results.

Figure 4 (a) shows typical vertical profiles of particle radius (r) and number density (N_p) at different times from the plasma ignition. These results were obtained using the iterative procedure of figure 2 (b), applied to vertical profiles extracted from the frames of figure 3 at electrode radius of 40 mm (shown on the frame at 93 s). Qualitatively similar results were also obtained at other radii.

Figure 4 (b) shows a time development of the powder layer thicknesses at the electrode axis, along with the particle radius and number density. Since the particles have to be tracked in space because of the layer dynamics, these results have been calculated at a variable height in the layer on the rf electrode side (also shown in figure 4 (b)).

3.1.1) Onset

From the scattering images in figure 3, one can clearly see that the powder spatial distribution throughout the plasma volume is separated into two layers over all the time development. This structure is already observed at the very onset of vertical scattering intensity (not shown in figure 3). At this time we estimate the particle radius to be around 5 nm. Moreover the 2-D scattered intensity then increases very uniformly in space up to 13.5 s which corresponds to the transition to Mie scattering [31]. Here the particulate radius is estimated to be around 15-20 nm, from the Rayleigh validity limit [31]. The scattering signals reveal, in-situ, a spatially-uniform size distribution of the particles during the early stage of their growth ($r < 20$ nm), since the scattered intensity in the Rayleigh approximation scales as $N_p r^6$ [31].

3.1.2) Agglomeration

In figure 3, at 18 and 21 s, there are some spatial inhomogeneities in which the scattered intensity is enhanced and the degree of polarisation (P) is less than one. By considering the corresponding particle radius (r) and number density (N_p) of figure 4 (a) at 19.5 s, one can see that these zones correspond to a rapid increase of particle size by agglomeration, suggested by the corresponding drop of N_p . This agglomeration phenomenon appears to start non-uniformly in space and figure 4 (b) shows that the particle radius growth rate exceeds 30 nm s^{-1} , which is too fast to be attributed to radical deposition or polymerisation mechanisms. The early detectable phase of growth by scattering has already been shown to be related to agglomeration by single beam scattering measurements [27] as well as by ex situ particle sampling [24, 29].

The physical mechanism which triggers this agglomeration remains unknown. However, we estimate the number of electrons Z carried by a particle to be at least ten [38] prior to agglomeration, and this must be neutralized for coalescence to occur. We suggest that one way for the particles to lose their charge is by a strong local perturbation to the plasma: since we empirically approximate the charge density carried by the particles to scale as $N_p r^q$ ($q > 1$) [38],

it could locally reach such high values (up to at least 10^{15} m^{-3} estimated from figure 4) that the free electron density may be locally depleted. The particle charge would then disappear whereupon particles could coalesce. Since the agglomeration process favors the reduction of particle-carried charge density, the plasma electron density could recover. In this way, the agglomeration may be triggered by crossing a limit of particle-carried charge density.

3.1.3) Uniform slow growth

In figure 3 at 21 to 60 s, two periods of bright/dark regions (of opposite phase for horizontal and vertical polarisations) are visible. This is due to the size-dependence of Mie scattering terms $|S_h|^2$ and $|S_v|^2$ in Eq. (1) and Fig. 2 (a) which convolute the total scattered intensities. For the high intensity contrasts observed, this proves that the particles which dominate the scattering grow uniformly over large regions of the plasma. Since P (in figure 2(a)) is a sensitive function of particle size, the spatial size distribution within a fringe is less than about 30 nm. This also reveals that scattering measurements for different polarisations are necessary for correct interpretation, because reduction of a single polarised scattered intensity may be misinterpreted as a reduction of powder quantity (see figure 5 below).

This spatial uniformity of size and number density within the powder layers is confirmed by the calculated profiles in figure 4 (a) from 34.5 to 72 s. During this period of uniform growth, we estimate from figure 4 (b) a particle radius growth rate of around 1.5 nm s^{-1} , resembling amorphous silicon deposition rates. During this phase, the refractive index approximates to that of highly-hydrogenated amorphous silicon. The corresponding number density falls slowly which we attribute to particle leakage as observed at the electrode edges (see figure 3). During the same time the powder layers contract and move slightly towards the electrode mid-gap. This shows that single beam light scattering experiments can be misleading for long time analyses because particles can drift out from the restricted observation volume.

During the whole particle development described here, the powder layers remain separate and are sharply delimited at the layer boundaries where the particle number density drops to near zero within 1 mm. We estimate the particle-carried charge to be around 10^{15} electrons m^{-3} and so the difference in free electron density on either side of the narrow boundary will be of the same order. These boundaries are possibly double layers which arise to match the transition in electron density and temperature between zones with and without powder [34, 35]. Insofar as the discontinuities are maintained, separate plasma regions with and without powder can evolve independently.

We estimated the inter-particle Coulomb coupling parameter Γ , described in ref [17], with an assumed particle temperature of 300 K (particles not much hotter than the gas temperature [39]) and Z estimated from ref [38] for the radii and number densities of figure 4(b). In the most pessimistic case ($T_e = 1 \text{ eV}$ $n_e = 0.1n_i$) we obtain $\Gamma = 5$ before agglomeration, and between 30 and 50 in the slow growth phase. This indicates that the particles are strongly

coupled which may explain why their density has to reduce while their size is continuously increasing ($\Gamma \propto Z^2 N_p^{1/3}$). The particle expulsion occurs in regions where potential trapping is weak or distorted, for example, in the fringing fields near the electrode edges. Strong coupling could also be responsible for the uniform spatial distributions observed. Supporting evidence for strong particle coupling is our observation of low frequency fluctuations of the scattered light and plasma emission after agglomeration phase. Such fluctuations have been attributed to density waves induced by collective interaction of the particles with the plasma [37].

3.1.4) Size segregation and new generations of particles

The last profile of figure 4 (a) ($t = 94.5$ s), shows a non-uniform size distribution, with the larger particles being segregated towards the plasma-sheath boundaries [25]. Nevertheless, the relative size gradient remains small (less than 50 nm for an average radius of 200 nm throughout a layer).

From figure 3 at nearly the same time, there are Rayleigh zones at the radial edge of each powder layer, which are the signature of very small particles (< 20 nm radius). Note that at 72 s no scattering was detected there for either polarisation. This possibly represents a new generation of particle formation [24, 29] which is visible here because of its separation from the existing powder layers: new small particles perhaps also grow in the powder layers, but scattering from these would in any case be dominated by scattering from the existing particles.

3.2) Steady-state plasmas with trapped powder

The time development described in the previous section covers 102 s from plasma ignition. After that, the particles continue to form and the powder structure evolves further. During this evolution, successive expansions and contractions of the powder layers are observed by 2-D scattering, together with the appearance and disappearance of spatial Mie interference fringes within each layer. In conditions where the powder production is not too high (low rf power), after 3 to 5 min the plasma/powder ensemble can reach a dynamic equilibrium in which the powder structure and fringes are frozen, even though the particles continue to form and leak out of the plasma volume. With high formation rates, the evolution described above can repeat periodically without reaching a steady state.

Figure 5 represents pseudocolor images of the 2-D scattering for both polarisations and the corresponding degree of polarisation along with the Rayleigh zones for three different steady-state plasma conditions. The first row represents the steady state of the pure silane plasma for which the time evolution has been described in the previous section. The second row is a 5 sccm silane flow diluted in 20 sccm argon in otherwise similar conditions. The third row of images is obtained by stopping the silane flow in this silane/argon steady-state plasma to leave powder trapped in an argon plasma. One can observe a striking modification of the overall powder structure by switching from silane/argon to pure argon. The powder structure changes

from two layers, similar to the pure silane case, to an annular structure. This transition occurs gradually during 2 min after the silane flow interruption, which may be related to the time necessary for purging of the remaining silane in the chamber. During this transition, the two powder layers slowly move towards each other at the periphery and in the center of the electrodes, ending with the stable annular structure shown in figure 5. The annular structure can be compared with the potential structure [40] computed by 2-D fluid models [6, 18].

If the silane flow is restored, the band-like structure reappears within 0.5 s. This indicates that the powder spatial distribution and trapping depends not only on reactor geometry but also on plasma composition. Moreover, the confinement of powder in two layers may be related to the electronegative character of silane-containing discharges [35].

In addition to the overall powder structures changes, well-defined spatial fringes are observed within the layers or annulus of the scattering images in Fig. 5. This fine structure is not due to complicated zones with or without powder, but reveals the scattered intensity convolution by size-dependent Mie scattering terms as evidenced by the corresponding degree of polarisation; the bright/dark regions are reversed for the horizontal/vertical polarisations. From Fig. 2 (a), these fringes show spatial size gradients of the particles which dominate the scattering. However, a unique determination of the size profiles would only be possible with multiple wavelengths because P is a multi-valued function and the direction in which the sizes increase is not known. During the transition from silane/argon to pure argon described above, the successive fringes move together without mixing, suggesting that the particles are strongly coupled and cannot freely move within the potential traps. In summary, the fringes in polarised scattering images reveal a spatial segregation of particle sizes.

3.3) Effects of powder on plasma optical emission

Spatially-resolved measurements of the plasma optical emission have often been performed for powder-containing discharges, either as a monitor of potential traps [6, 41] or as a sign of a discharge regime transition [16, 42]. No account was made for the possible extinction of the measured emission by particles located in the optical path to the detector.

In this section we consider the absorption and scattering of the plasma emission by the particle clouds. In figure 6 (a) we represent the measured SiH^* emission profiles on the electrode axis, along with laser extinction for different times after plasma ignition. Initially, the measured emission profile is slightly peaked near the plasma-sheath boundaries, indicating that electron heating is due to wave-riding (α -mode [42]). At $t = 13.5$ s, the SiH^* profile shape has changed and the emission intensity has increased by more than a factor of two. Up to this time the extinction is still below the measurement limit and even if the powder is already detectable by scattering, the emission is not expected to be attenuated by the particles. For later times (at $t = 18, 39$ and 72 s in figure 6 (a)), plasma emission and laser extinction, although their source

and path are different, show spatial correlations which suggests that extinction by the powder could induce a significant modification to the emission profile.

To test the above suggestion, we performed a simple modelling of the rôle of extinction on plasma emission by assuming a homogeneous local emission coefficient $\Delta I_{\text{SiH}}(y, z) = 1$ over all the plasma volume and zero elsewhere. For these conditions the emission intensity vertical profile on the electrode axis is given by [43] :

$$I_{\text{SiH}}(z) \propto \int_{-R}^R \Delta I_{\text{SiH}}(y, z) \exp\left(-\int_y^R \epsilon(\sigma, z) d\sigma\right) dy \quad (4)$$

where R is the path length from the plasma axis to the detector and $\epsilon(\sigma, z) = N_p(\sigma, z) C_{\text{ext}}(\sigma, z)$ is the local extinction coefficient. Accurate iterative inversion procedures [43] require the local extinction coefficient $\epsilon(\sigma, z)$ to be determined with a separate measurement of the extinction throughout the plasma volume. Here we simplify by assuming an extinction coefficient $\epsilon = \epsilon_0$ to be constant in powder regions determined from the 2-D scattering measurements and zero elsewhere :

$$I_{\text{SiH}}(z) \propto \int_{-R}^R \Delta I_{\text{SiH}}(y, z) \exp(-\epsilon_0(y, z)(R-y)) dy \quad (5)$$

ϵ_0 is determined so as to approximate the measured laser extinction profile using equation (2) in section 2.2.

Figure 6 (b) represents $I_{\text{SiH}}(z)$ with and without extinction included, the measured and reproduced laser extinctions, and the Abel-inverted SiH* emission profile (measurement), corresponding to $t = 28.5$ s on figure 3. The best agreement of the calculated laser extinction is obtained for $\epsilon_0 = 0.015 \text{ mm}^{-1}$, which is physically reasonable for the particle size and number density obtained in section 3.1.3. The simulated emission profile (I_{SiH}) with powder shows a strong reduction (by more than a third in the regions of the powder layers) with respect to the case without powder. We conclude that the measured emission profile is significantly modified due to the localised extinction by the powder layers. This shows that in the case of a high number density of particles with radius of about 100 nm, dusty plasmas should be treated as optically thick media. As a consequence, a straightforward interpretation of measured emission profiles can be misleading, since in the case of figure 6 (b) the local plasma emission coefficient is certainly higher in the regions of powder layers. This is consistent with observation and modelling of enhanced electron temperature [34] and electric field [16] in regions containing particles. The fact that the emission starts to increase globally before the powder is visible by scattering (figure 6 (a)) is a sign that small particles ($r < 15$ nm) already have an important effect on the electron energy distribution.

4) CONCLUSIONS

A polarised, beam-expanded laser was used to investigate spatio-temporal powder formation and trapping in silane plasmas by monitoring the scattered and transmitted light with CCD cameras. The scattered intensity shows alternate bright/dark regions in time and space which reverse according to the polarization; these are attributed to convolution by the particle size-dependence of the Mie scattering terms. The temporal variations show uniform particle growth over large regions of the powder layers. High contrast spatial intensity variations (fringes) demonstrate the existence of particle size gradients for steady-state silane plasmas and for powder trapped in an argon plasma; the difference in the trapping topography reveals the importance of plasma chemistry in determining powder location.

Self-consistent estimations of particle size and number density were made throughout the discharge volume during particle growth and agglomeration. These suggest that strong Coulomb coupling influences the powder dynamics and should be included in the understanding of high particle density plasmas. Plasma emission profiles should be corrected for extinction by powder.

In conclusion, these techniques provide quantitative experimental data for comparison with plasma/particle modelling.

ACKNOWLEDGMENTS

The authors gratefully acknowledge W. Schwarzenbach and L. Sansonnens for their contribution to this work. We also thank B. Duval, R. Pitts and M. Corboz for providing the digitization system and technical assistance. This work was funded by Swiss Federal Research Grant EF-REN(93)035, and BBW93.0136 for BRITE-EURAM project BE-7328.

REFERENCES

- [1] G. S. Selwyn, J. E. Heidenreich and K. L. Haller, *J. Vac. Sci. Technol. A* **9**, 2817 (1991); and G. S. Selwyn *Semicond. Int.* **16**, March 72 (1993).
- [2] N. Braithwaite and B. Graham, *New Scientist* **140**, November 27 (1993); and A. Bouchoule, *Phys. World* **6**, August 47 (1993).
- [3] P. Ho, R. S. Buss and R.E Loehman *J. Mater. Res.* **4**, 973 (1989); and H. Anderson, T. T. Kodas and D. M. Smith, *Ceram. Bull.* **68**, 996 (1989).
- [4] J. Perrin and J. P. M. Schmitt, *Proc. 11th European Photovoltaic Solar Energy Conf.*, ed. L Gimaraes et al (Coire, Switzerland : Harwood), p 80 (1992).
- [5] S. J. Choi and M. J. Kushner, *J. Appl. Phys.* **74**, 853 (1993).
- [6] See papers in NATO Advanced Research Workshop on Formation, Transport and Consequences of Particles in Plasmas, published in *Plasma Sources Sci. Technol* **3**, 239-451 (1994).
- [7] See papers in Special Issue on Charged Dust in Plasmas, published in *IEEE Trans. Plasma Sci.* **22** (2), 89-179 (1994).
- [8] J. E. Daugherty, R. K. Porteous, M. D. Kilgore, and D. B. Graves, *J. Appl. Phys.* **72**, 3934 (1992).
- [9] R. N. Nowlin and R. N. Carlile, *J. Vac. Sci. Technol. A* **9**, 2825 (1991).
- [10] S. J. Choi and M. J. Kushner, *J. Appl. Phys.* **75**, 3351 (1994); and *Appl. Phys. Lett.* **62**, 2197 (1993).
- [11] T. J. Sommerer, M. S. Barnes, J. H. Keller, M. J. McCaughey and M. J. Kushner, *Appl. Phys. Lett.* **59**, 638 (1992).
- [12] M. S. Barnes, J. H. Keller, J. C. Forster, J. A. O'Neill and D. K. Coultas, *Phys. Rev. Lett.* **68**, 313 (1992).
- [13] J. E. Daugherty, R. K. Porteous and D. B. Graves, *J. Appl. Phys.* **73**, 1617 (1993).
- [14] M. D. Kilgore, J. E. Daugherty, R. K. Porteous, and D. B. Graves, *J. Appl. Phys.* **73**, 7195 (1993)
- [15] M. J. McCaughey and M. J. Kushner, *J. Appl. Phys.* **69**, 6952 (1991).
- [16] J.-P. Boeuf and Ph. Belenguer, *J. Appl. Phys.* **71**, 4751, (1992); and *J. P.Boeuf, Phys. Rev. A* **46**, 7910 (1992).
- [17] H. Ikesi, *Phys. Fluids.* **29**, 1764 (1986).
- [18] J.-P. Boeuf, Ph. Belenguer, and T. Hbid, *Proc. XXIth Int. Conf. on Phenomena in Ionised Gases* (Bochum, Germany), 108 (1993); and in ref [6]
- [19] H. Kausche and R. D. Plättner, *Proc. XXIth European Photovoltaic Solar Energy Conf.*, ed. L. Gimaraes et al (Coire, Switzerland : Harwood), p 195 (1992).
- [20] G. M. Jellum, J. E. Daugherty and D. B. Graves, *J. Appl. Phys.* **69**, 6923 (1991).
- [21] R. N. Carlile, J. F. O'Hanlon, L. M. Hong, M. P. Garrity, and S. M. Collins, in ref [6]
- [22] K. G. Spears, T. J. Robinson and R. M. Roth, *IEEE Trans. Plasma Sci.* **14**, 179 (1986).

- [23] A. Bouchoule, A. Plain, L. Boufendi, J.-Ph. Blondeau and C. Laure, *J. Appl. Phys.* **70**, 1991 (1991).
- [24] L. Boufendi, A. Plain, J.-Ph. Blondeau, A. Bouchoule, C. Laure, and M. Toogood, *Appl. Phys. Lett.* **60**, 169 (1992).
- [25] G. M. Jellum and D. B. Graves, *Appl. Phys Lett.* **57**, 2077 (1990).
- [26] G. Spears, R. P. Kampf, and T. J. Robinson, *J. Phys. Chem.* **92**, 5297 (1988).
- [27] Ch. Hollenstein, J.-L. Dorier, J. Dutta, L. Sansonnens, and A. A. Howling, in ref [6]
- [28] Y. Watanabe, and M. Shiratani, in ref [6]
- [29] L. Boufendi, and A. Bouchoule, in ref [6]
- [30] W. Böhme, W. E. Köhler, M. Römheld, S. Veprek, and R. J. Seebök, in ref [7]
- [31] C. F. Bohren and D. R. Huffman, "Absorption and Scattering of Light by Small Particles", Wiley New York 1983.
- [32] A. A. Howling, Ch. Hollenstein and P.-J. Paris, *Appl. Phys. Lett.* **59**, 1409 (1991).
- [33] R. J. Seeböck, W. Böhme, W. E. Köhler, M. Römheld, and S. Veprek, in ref [6]
- [34] S. G. Geha, R. N. Carlile, J. F. O'Hanlon, and G. S. Selwyn, *J. Appl. Phys.* **72**, 374 (1992); and R. N. Carlile, and S. G. Geha, *J. Appl. Phys.* **72**, 4785 (1993)
- [35] A. Garscadden, *Proc. XXth Int. Conf. in Ionised Gases (Pisa)*, Invited Paper (1991) p147, and A. Garscadden, and in ref [6].
- [36] A. Bouchoule, and L. Boufendi, in ref [6].
- [37] J. H. Chu, Ji-Bin Du, and Lin I, *J. Phys. D : Appl. Phys.* **27**, 296 (1994).
- [38] D. B. Graves, J. E. Daugherty, M. D. Kilgore, and R. K. Porteous, in ref [6]; and J. Goree, in ref [6].
- [39] J. E. Daugherty, and D. B. Graves, *J. Vac Sci. Technol. A* **11**, 1126 (1993).
- [40] T. Hbid and J.-P. Boeuf, private communication.
- [41] M. Dalvie, G. S. Selwyn, M. Surenda, C. R. Guarnieri, and J. J. McGill, *Appl. Phys. Lett.* **63**, 3279 (1993).
- [42] J. Perrin, C. Böhm, R. Etemadi, and A. Lloret, in ref [6], and references therein.
- [43] R. Rompe, and M. Steenbeck, "Progress in Plasmas and Gas Electronics", Vol. 1, Akademie-Verlag Berlin 1975.

FIGURE CAPTIONS

FIG 1: Schematic top and front scale views of the experimental arrangement, showing the plasma reactor and the expanded laser scattering and extinction measurement set-up. A1 and A2 represent rectangular apertures, P1 and P2 polarizers, W reactor windows, ND and IF neutral density and interference (487.3 nm bandwidth 11 nm) filters respectively.

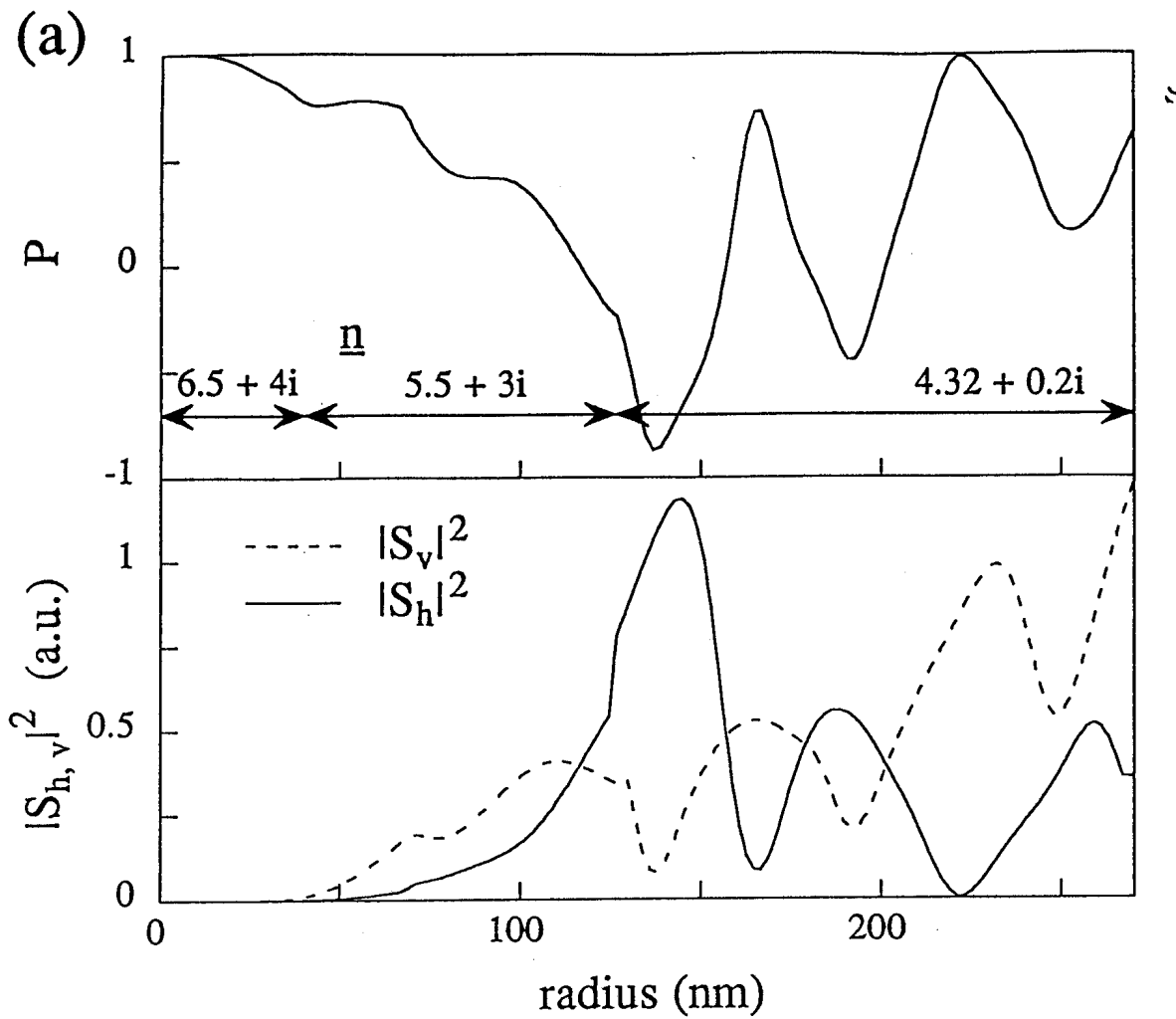
FIG 2: (a) Simulation of the degree of polarisation P , and relative scattering intensities $|S_h|^2$ and $|S_v|^2$ for both vertical and horizontal polarisations as a function of particle radius, with the corresponding size-dependent refractive index, \underline{n} . (b) Diagram of the iterative procedure followed to determine the particle radius, number density and refractive index.

FIG 3: Array of pseudo-color images of the measured 2-D scattering intensity profiles W_h , W_v from the powder layers in the electrode gap with the corresponding vertical normalised extinction profiles and 2-D image constructions of the degree of polarisation profiles P , with delimited "Rayleigh zones" (particle radius < 20 nm). Successive rows in the array correspond to different times from plasma ignition. Only half of the 2-D profiles are represented for convenience. Plasma parameters: 30 sccm silane at 0.1 mbar, rf power 5 W, laser power $8W\text{ cm}^{-2}$.

FIG 4: (a) Particle radius and number density vertical profiles at 40 mm from the electrode axis (see Fig. 3) for different times from plasma ignition, calculated using the iterative method described in section 2.3. (b) Time development of the powder layer position, particle radius and number density. These data were calculated by tracking powder in the lower layer at the electrode axis (vertical position shown along with the powder layer thickness evolution).

FIG 5: Array of pseudo-color images of the measured 2-D scattering intensity profiles W_h , W_v and the corresponding 2-D image constructions of the degree of polarisation profiles P , with delimited "Rayleigh zones" (particle radius < 20 nm) for steady state plasmas. The P construction enhances fringe contrast and eliminates the N_p dependence; the P fringes are therefore contours of constant particle size. Plasma conditions: pure silane 30 sccm at 5 W; silane/argon at 5/20 sccm ; and powder trapped in 20 sccm of argon.

FIG 6: (a) Comparison of measured SiH^* emission and laser extinction profiles at different times from plasma ignition. (b) Measured and simulated SiH^* emission intensity (with and without extinction due to powder, see text), along with measured and reproduced laser extinction vertical profiles at the electrode axis. Plasma conditions as for Fig. 3.



(b)

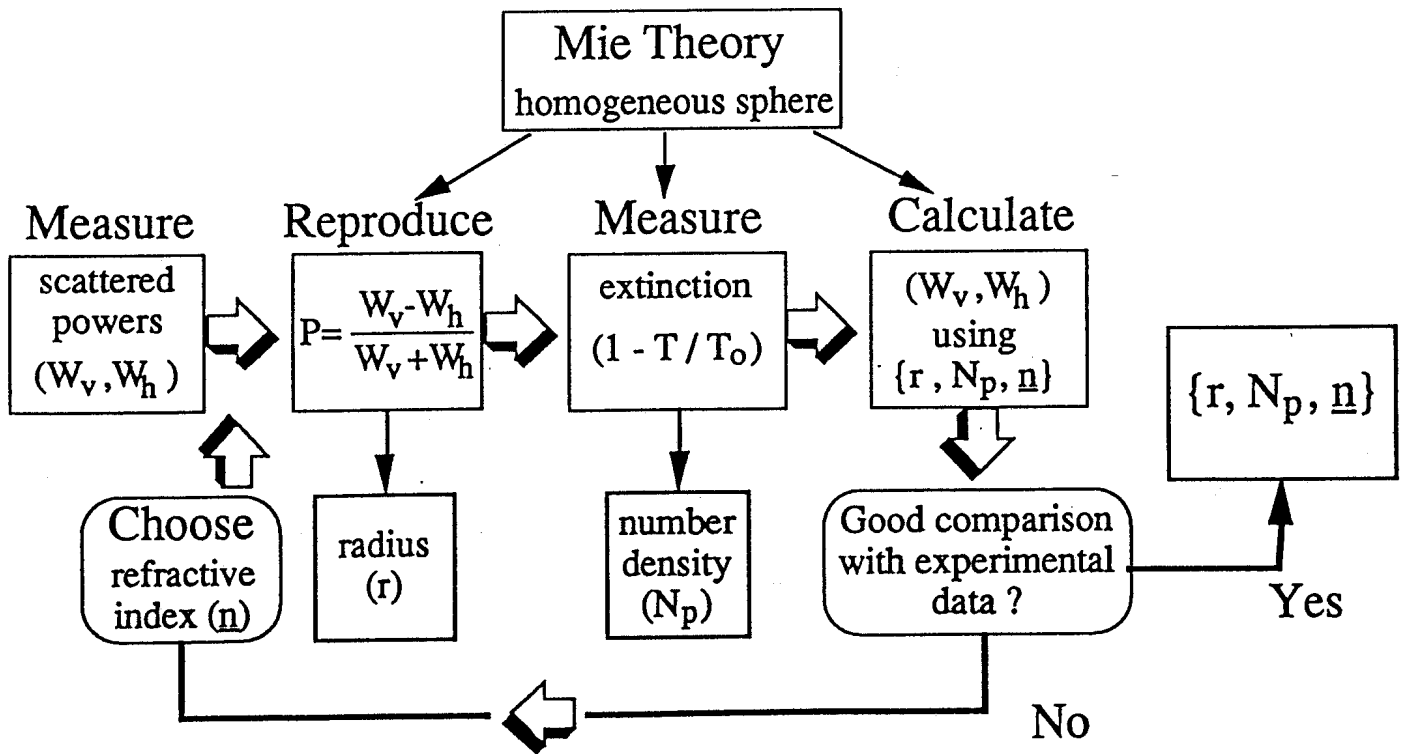


Fig. 2

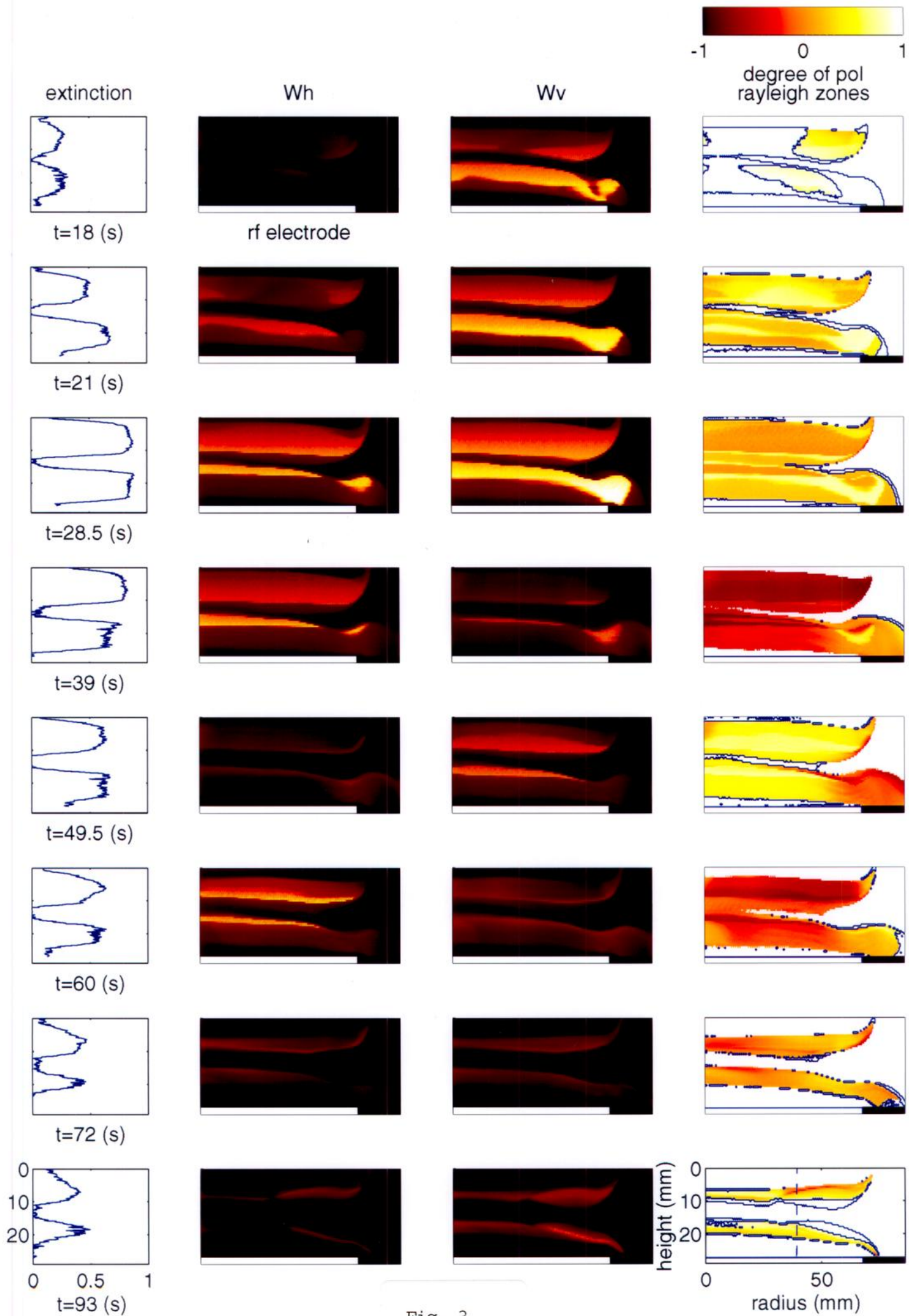


Fig. 3

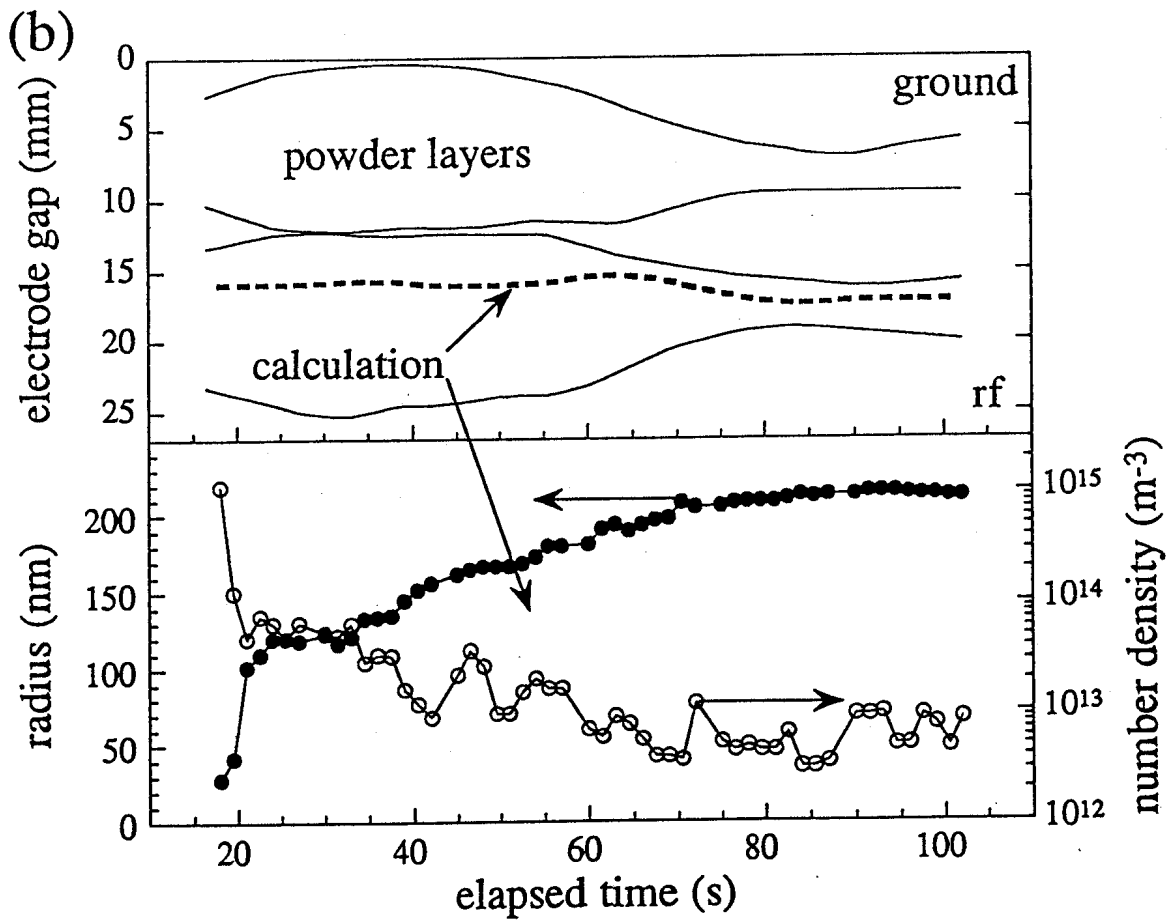
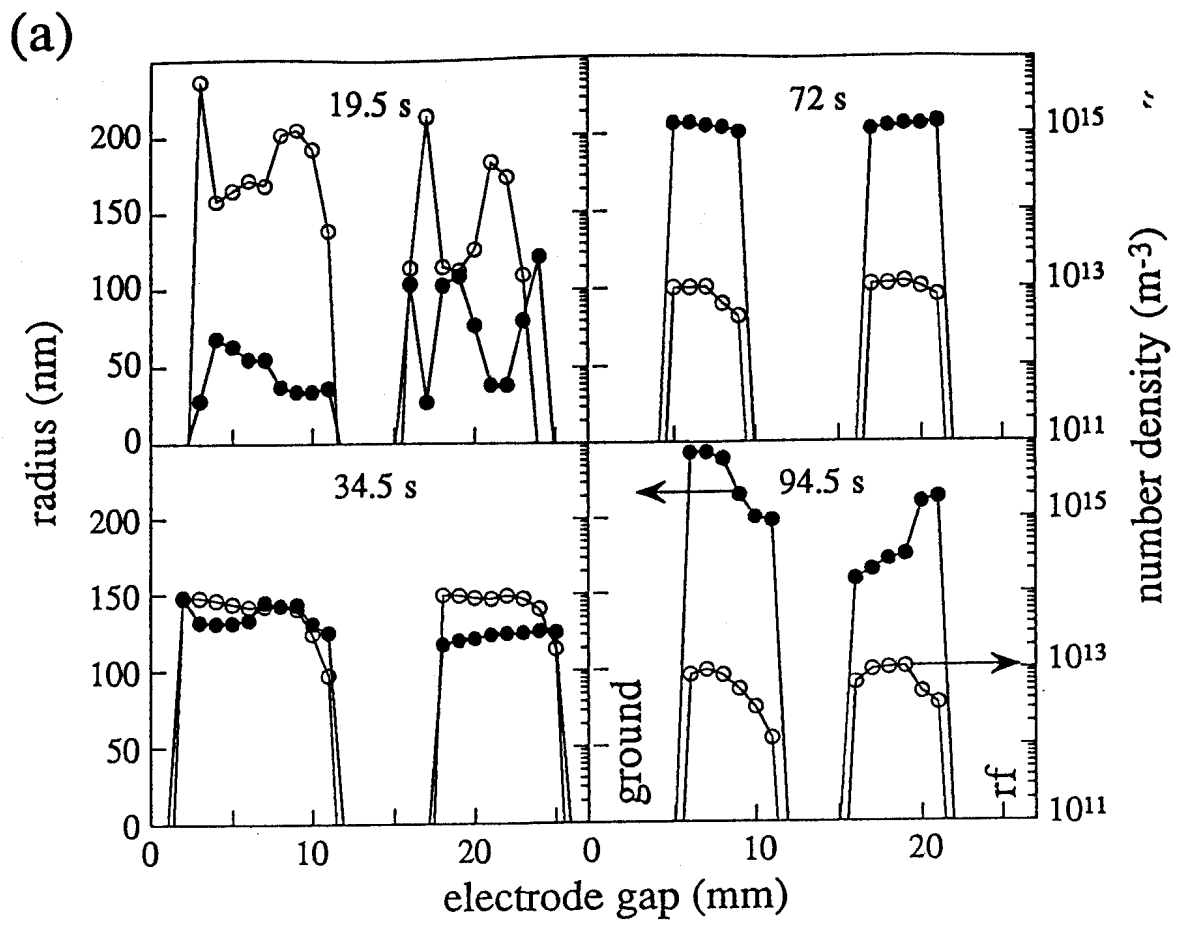


Fig. 4

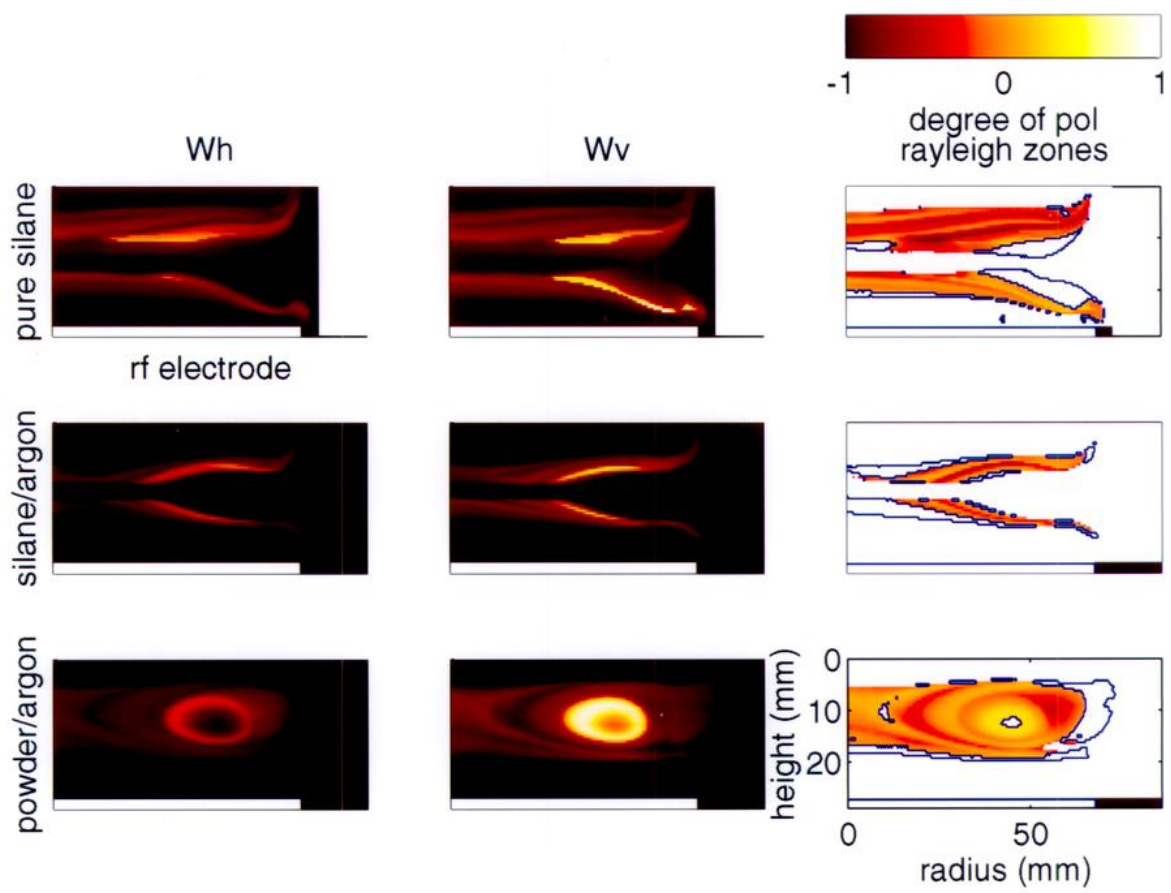


Fig. 5

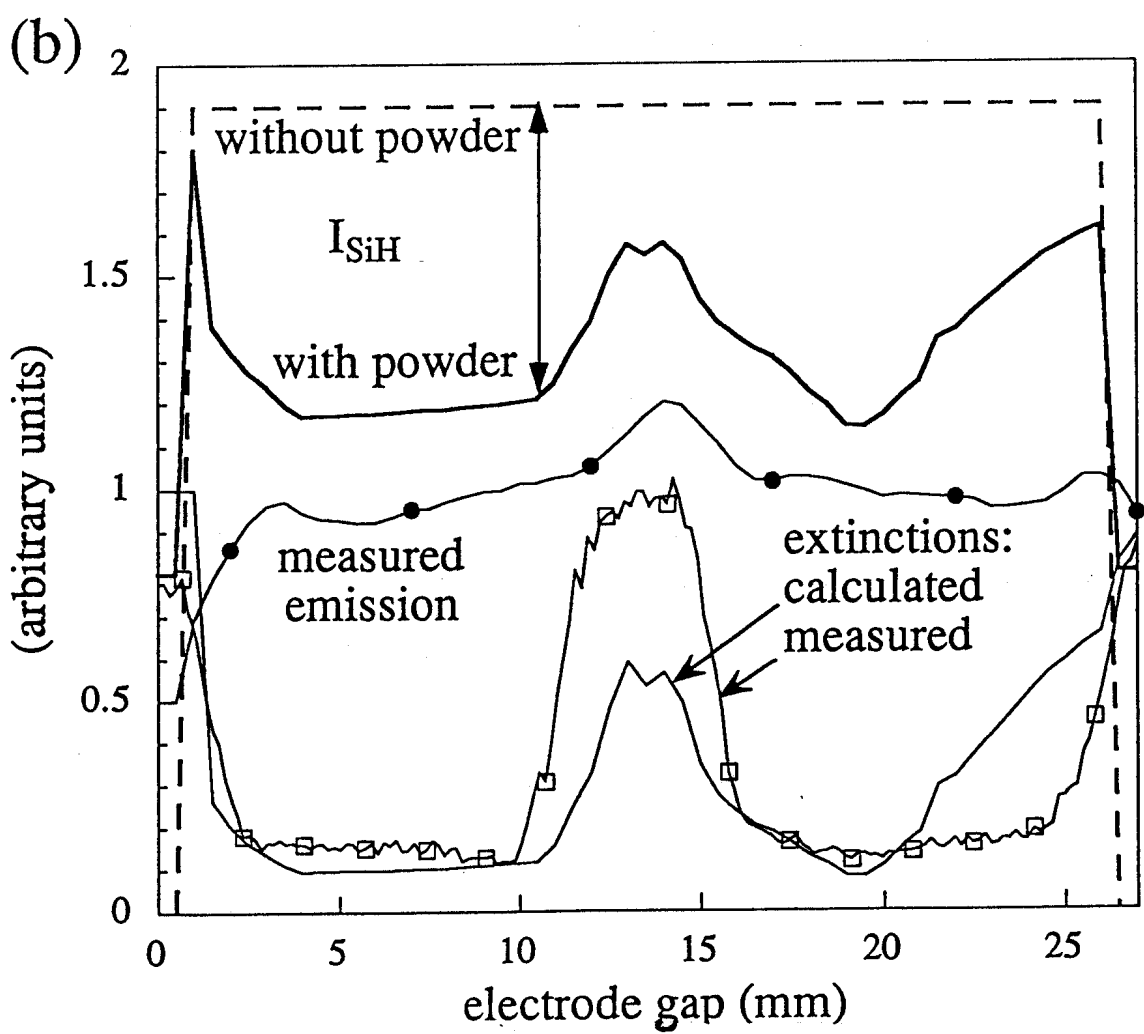
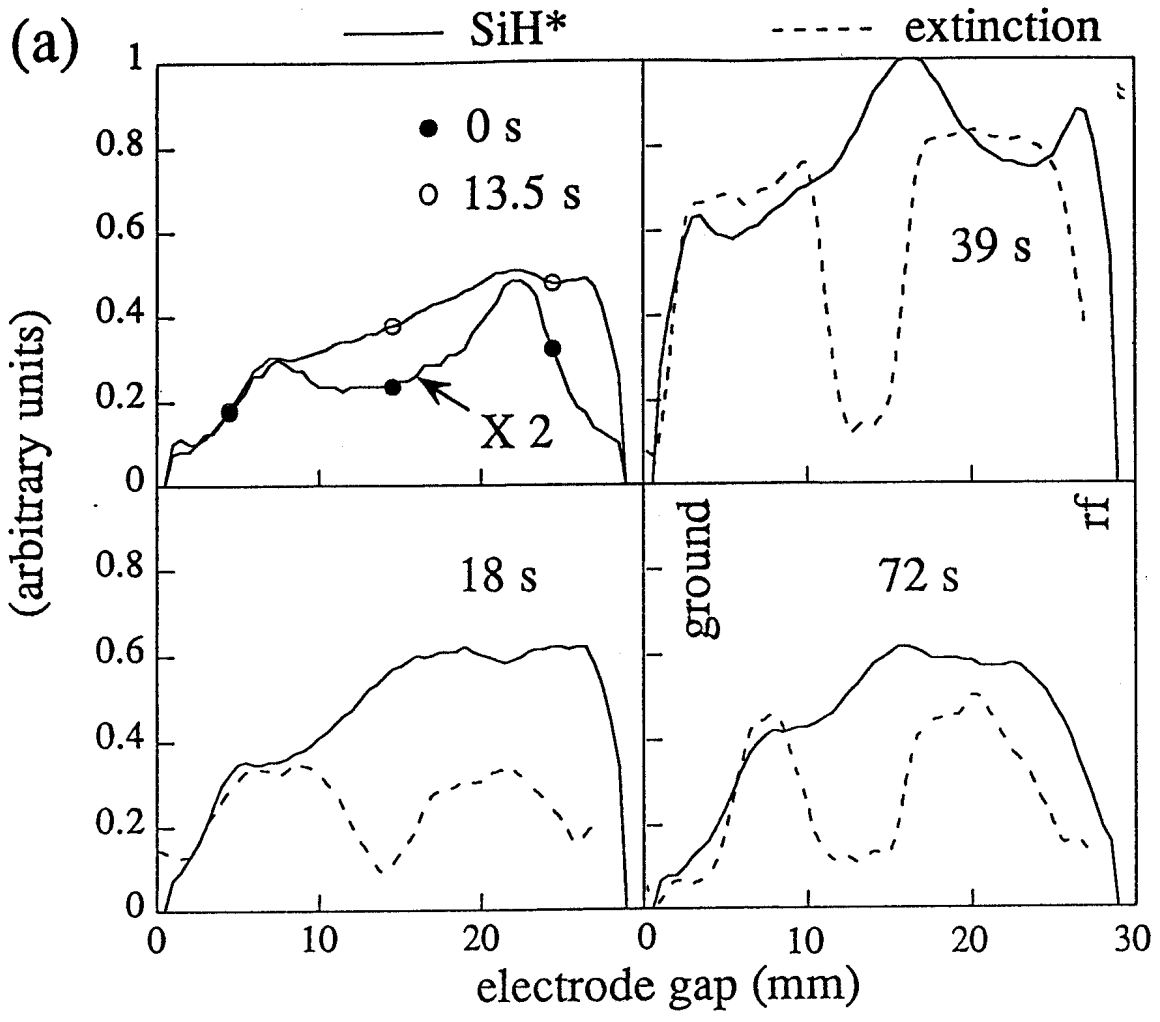


Fig. 6